Journal of Scientific Computing (2023) 97:31
https://doi.org/10.1007/s10915-023-02347-7

# A Modified A Posteriori Subcell Limiter for High Order Flux Reconstruction Scheme for One-Dimensional Detonation Simulation

**Shiwei Liu**[1,3] · **Li Yuan**[2,3]

Received: 2 May 2023 / Revised: 8 August 2023 / Accepted: 1 September 2023 /
Published online: 21 September 2023


**Abstract**
In this paper, a modified a posteriori limiter is developed for high order flux reconstruction (FR) scheme for the numerical simulation of detonation problems. In this limiting procedure, the unlimited FR solution at the new time step will be checked first by using some detection criteria, then the solution in the troubled cells are recomputed with a robust subcell finite volume (FV) scheme. The detection criteria for identifying troubled cells consist of the physical admissibility (e.g., positivity of density and pressure) and numerical admissibility (e.g., non-oscillating). We modify the detection criteria by using the KXRCF shock detector prior to the relaxed discrete maximum principle. This can track the troubled cells near strong shocks consecutively so as to improve the steady state convergence and can reduce the number of overly marked troubled cells. The subcell correction procedure endows the high order FR scheme the capability to capture discontinuities inside a cell without generating spurious oscillations. A series of one-dimensional numerical tests are carried out to assess the effectiveness of the proposed limiter. In particular, one-dimensional detonation wave problems with the overdriven factor $f = 1.8$–$1.3$ are calculated using third to sixth order accurate FR schemes in conjunction with the first order Godunov or second order TVD subcell FV scheme. It is shown that the FR schemes with the present a posteriori limiter can compute strong detonation waves robustly, and the third order FR scheme with the second order TVD subcell FV limiter has better resolution of detonation waves compared with the fifth order WENO-Z scheme under same degree of freedoms.

✉ Shiwei Liu
liusw@lsec.cc.ac.cn

Li Yuan
lyuan@lsec.cc.ac.cn

1 Institute of Applied Physics and Computational Mathematics, China Academy of Engineering Physics, Beijing 100094, China

2 ICMSEC and LSEC, Academy of Mathematics and Systems Science, Chinese Academy of Sciences, Beijing 100190, China

3 School of Mathematical Sciences, University of Chinese Academy of Sciences, Beijing 100190, China

**Keywords** Flux reconstruction method · a posteriori subcell limiter · Detonation wave · Steady state convergence

## 1 Introduction

Detonation wave problems have complicated fine structures and strong discontinuities. Numerical simulations of detonation wave problems necessitate the use of robust high order and high resolution schemes which can simultaneously resolve small-scale smooth structures and capture strong discontinuities without producing numerical oscillations robustly [1]. However, the tight coupling between the strong shock and the narrow reaction zone in detonation waves poses a challenge to high order numerical schemes.

Over the past two decades, many kinds of high resolution and high order numerical methods have been applied to numerical simulation of detonation phenomena. Henshaw et al. [2] applied a second order Godunov method to simulate detonation problems in which the chemistry is modeled with a three-step reaction model. To resolve the fine temporal and spatial scales near detonation fronts, they used overlapping grids and block-structured adaptive mesh refinement. Hu [3] proposed an h-adaptive finite volume (FV) method with a linear reconstruction and a weighted essentially non-oscillatory (WENO) limiter for the reactive Euler equations on unstructured triangular grids. Andrew et al. [4] used the fifth order WENO-M scheme together with a fifth order Runge–Kutta (RK) method to simulate pulsating one-dimensional (1D) detonations. Gao et al. [5] compared three versions of fifth order WENO finite difference schemes in the simulation of stable and unstable 1D detonations. Wang et al. [6] developed a high order positivity-preserving discontinuous Galerkin (DG) scheme for the reactive Euler equations to compute gaseous detonations in complex geometrical configurations. Zhu et al. [1] extended an $h$-adaptive RKDG method to 1D detonation wave simulations.

Proposed first by Huynh [7], the flux reconstruction (FR) method is a new class of high order methods for hyperbolic conservation laws, which allows several kinds of high order methods, including nodal DG [8] and spectral difference (SD) methods [9, 10], to be cast within a single framework. Like DG methods, FR methods preserve the property of compactness in space, i.e., only face neighbors are needed to calculate common numerical fluxes, enabling efficient implementation on modern parallel computers [11–13]. But unlike DG methods, FR methods are based on the differential form of governing equations, which makes the methods quadrature free and less expensive. To achieve arbitrary high order of accuracy, the FR solution is first approximated by interpolation of solution variables at the solution points in each grid cell and a flux function which is defined by a similar interpolation. Generally, this flux function is discontinuous across cell interfaces since it does not account for interactions between adjacent cells. Then a correction function $g$ associated with a cell interface of the current cell is employed to obtain a continuous flux function which returns common numerical fluxes at the flux points on the cell interface. Different FR methods are characterized by different choices of the correction function. Huynh [7] proposed several correction functions such as $g_{\mathrm{DG}}$ which makes the FR method equivalent to the nodal DG method and the lumped correction function $g_2$ which makes the flux derivative correction only appear at cell interfaces. Jameson [14] proved that the SD schemes are energy stable for 1D linear advection problems by using energy estimates and a norm of Sobolev type. By using the same technique, Vincent et al. [15] identified a family of energy stable FR schemes

for 1D linear advection problems where the correction function is a one-parameter linear combination of three Legendre polynomials.

Wang and Gao [16] shown that the flux derivative correction in the FR method [7] can be realized by using a correction field, and the resulting method was named as Lifting Collocation Penalty (LCP) method [16]. Later, Yu and Wang [17] uncovered the relationship between LCP and FR. Due to the tight connection between FR and LCP, the involved authors combined the names and called them CPR (Correction Procedure via Reconstruction) method. For a comprehensive review of FR methods, we recommend [18] and the references therein.

Being a high order linear upwind scheme in the sense of Godunov approach [19], the FR method may generate spurious oscillations in the presence of discontinuities, which may lead to nonlinear instability, and eventual blowup of simulation. Thus, shock stabilization techniques are needed to control numerical oscillations. There are three main approaches to stabilization of FR methods: local artificial dissipation (LAD) [20], limiting, and h-p adaption [18]. The LAD approach [20] needs an additional reconstruction for the auxiliary variable $q = \nabla u$, which is not economical, and it has problem-dependent empirical parameters. The h-p adaption approach [18] is sophisticated and can only stabilize weak discontinuities. As for the limiting approach, there is less work, though a lot of limiters have been developed for high order FV and DG methods, such as TVD limiters [21, 22], TVB limiters [23], MLP limiter [24, 25], moment limiters [26–29], WENO and HWENO limiters [30–34].

However, all of the aforementioned limiters are *a priori* in the sense that only the data at time $t^n$ are used to perform the detection and limiting process, and then the limited solution is advanced to time $t^{n+1}$. Thus, the "worst case scenario" has to be considered as a precautionary principle. A supplement to the *a priori* limiter is required for calculating extreme cases, for example, Zhang and Shu [35, 36] and others [37] have developed positivity-preserving limiters to maintain the positivity of density and pressure for gas dynamical problems. On the other side, Diot et al. [38, 39] constructed an iterative *a posteriori* limiting technique (MOOD, Multi-dimensional Optimal Order Detection) for high order FV method. In this technique, the unlimited high order FV scheme is first used to calculate a candidate solution at time $t^{n+1}$, then a detecting procedure is carried out to detect troubled cells which do not respect some stability criteria, including the physical admissibility and the numerical admissibility. After that, the polynomial degree in a troubled cell and its neighbor cells is reduced by one or more order and the low order numerical solution in these cells are recalculated, and the result will be checked again. This *try and fail* algorithm will not finish until the solution is acceptable. Inspired by the MOOD idea [38, 39], Dumbser et al. [40, 41] and Vilar [42] developed *a posteriori* limiting techniques for DG methods, in which the solution in a troubled cell at the previous time $t^n$ is distributed to the underlying subcells, and a more robust scheme is used to recalculate the subcell solutions at $t^{n+1}$ and finally the subcell solutions are assembled to form the acceptable high order DG solution at $t^{n+1}$ in the troubled cell. The *a posteriori* limiter can suppress numerical oscillations and at the same time preserve positivity of density and pressure automatically [40, 41]. Nevertheless, extensions of a posteriori limiters to FR methods are few [42, 43].

In this paper, we combine a version of FR scheme [15] with a modified *a posteriori* subcell limiter for simulating 1D gaseous detonation. To the best of our knowledge, this is the first time that a FR method is applied to detonation simulations. In our limiting process, the unlimited FR scheme is first used to calculate the candidate solution, then the physical admissibility detection (PAD) (negative density and pressure in gas dynamics, float NaN) is carried out. For regions with physically admissible solution, the numerical admissibility detection (NAD) is carried out. But unlike the NAD procedure [39, 40, 42] which only uses the relaxed discrete maximum principle (DMP), we first use the KXRCF (abbreviation of the authors [44]) shock

detector to classify the regions into smooth, intermediate, and discontinuous regions. For smooth regions, the candidate solution is accepted. For discontinuous regions, the cells are directly marked as troubled cells. For intermediate regions, the detection using the relaxed DMP is further carried out. After that, the solution in all the troubled cells are recalculated by using a robust subcell finite volume scheme, in which the initial subcell averages are projected from the FR solution in the troubled cells at the previous time step. Finally these updated subcell averages will be gathered back into a high order FR polynomial via a subcell reconstruction procedure. The numerical tests show that the FR scheme with the modified *a posteriori* subcell limiter can compute a high resolution discontinuous solution within a cell. Particularly, the modified *a posteriori* limiter performs remarkably well in simulations of steady state detonation problems.

The remainder of this paper is organized as follows. Section 2 gives the FR scheme used. Section 3 describes in detail the modified *a posteriori* subcell finite volume limiter for the FR scheme. Section 4 gives the governing equations for 1D gaseous detonations and typical ZND solution profiles which will be used as the initial conditions. Section 5 presents a series of typical numerical tests including detonation problems to assess the effectiveness of the FR scheme combined with the modified a posteriori limiter. Conclusions are drawn in Sect. 6.

## 2 Unlimited FR Method

In this section, the FR method is introduced briefly. For a detailed introduction, the review article by Huynh et al. [18] and the references therein are recommended. This section is organized as follows: in 2.1, we describe the FR method [7] for 1D scalar conservation laws bearing in mind that the extension to systems is in the component-by-component fashion; in 2.2, we discuss the choice of the correction function and solution points, which finally determines the unlimited 1D FR scheme used in this paper.

### 2.1 FR Method for 1D Scalar Conservation Law

Consider the 1D scalar hyperbolic conservation law

$$\frac{\partial u}{\partial t} + \frac{\partial f}{\partial x} = 0 \tag{1}$$

in the computational domain $\Omega$, where $x$ is the spatial coordinate, $t$ is the time, $u = u(x, t)$ is a conserved scalar, and $f = f(u)$ is the flux function of $u$. The domain $\Omega$ is partitioned into $N_{\text{elem}}$ non-overlapping elements (cells) with an element being $\Omega_i = \{x \mid x_{i-1/2} \le x \le x_{i+1/2}\}$ such that

$$\Omega = \bigcup_{i=1}^{N_{\text{elem}}} \Omega_i. \tag{2}$$

For the convenience of implementation, the element $\Omega_i$ is transformed into the reference element $\hat{\Omega} = \{r \mid -1 \le r \le 1\}$ via the mapping

$$r = \Gamma_i(x) = 2\left(\frac{x - x_{i-1/2}}{x_{i+1/2} - x_{i-1/2}}\right) - 1, \tag{3}$$

which has the inverse transformation

$$x = \Gamma_i^{-1}(r) = \frac{1-r}{2}x_{i-1/2} + \frac{1+r}{2}x_{i+1/2}. \tag{4}$$

With the mappings, Eq. (1) can be transformed into a conservation equation on the reference element as follows,

$$\frac{\partial \hat{u}}{\partial t} + \frac{\partial \hat{f}}{\partial r} = 0, \tag{5}$$

where

$$\hat{u} = \hat{u}(r,t) = u(\Gamma_i^{-1}(r), t), \tag{6}$$

$$\hat{f} = \hat{f}(r,t) = \frac{f(\Gamma_i^{-1}(r), t)}{J_i}, \tag{7}$$

and $J_i = \frac{\partial x}{\partial r} = \frac{x_{i+1/2}-x_{i-1/2}}{2}$ is the Jacobian of the mapping function. From now on, all calculations are performed on the reference element $\hat{\Omega}$. To simplify notations, when there is no confusion the element index $i$ will be dropped.

The solution $\hat{u}$ is approximated with piecewise polynomials. To get a $(K+1)$th-order accurate approximation of $\hat{u}$, the FR method requires $(K+1)$ data $\hat{u}_j^\delta(t)$ at locations $r_j$, $j = 0, \ldots, K$ in the reference element which are called solution points and will be given later in the end of 2.2. A $K$th degree polynomial approximation for the solution on the reference element can be constructed via the Lagrange interpolation,

$$\hat{u}^\delta(r,t) = \sum_{j=0}^{K} \hat{u}_j^\delta(t) l_j(r), \tag{8}$$

where $l_j$ is the $j$th Lagrange polynomial on the reference element defined as

$$l_j(r) = \prod_{k=0, k\neq j}^{K} \left(\frac{r-r_k}{r_j - r_k}\right). \tag{9}$$

Similarly, a $K$th degree polynomial approximation $\hat{f}^{\delta \mathrm{D}}$ for the transformed flux can be constructed using the same technique

$$\hat{f}^{\delta \mathrm{D}}(r) = \sum_{j=0}^{K} \hat{f}_j^\delta l_j(r), \tag{10}$$

where $\hat{f}_j^\delta = \hat{f}(\hat{u}_j^\delta)$ are nothing but the value of the transformed flux at the solution point $r_j$, evaluated directly from the point solution $\hat{u}_j^\delta$ using Eq. (7). Notice that the superscript $\delta$ means discrete and D means discontinuous [15].

However, the flux interpolation function (10) is a piecewise polynomial and is discontinuous at cell interfaces. It does not include the interaction of the data between adjacent elements. Further, since $\hat{u}^\delta$ is a $K$th degree polynomial, the time derivative term in Eq. (5) is a polynomial of degree $K$, whereas $\partial \hat{f}^{\delta \mathrm{D}}/\partial r$ is of degree $K-1$ and thus it is not consistent with the time derivative term.

To fix these two drawbacks, a continuous flux function $\hat{f}^\delta$, which approximates the piecewise polynomial flux function $\hat{f}^{\delta \mathrm{D}}$ in some sense, must be constructed. The requirements for $\hat{f}^\delta$ are that it should take the unique numerical flux value at the element interface, and be one

order higher than $\hat{f}^{\delta \mathrm{D}}$ [7]. Instead of defining $\hat{f}^{\delta}$ directly, the correction flux $\hat{f}^{\delta \mathrm{C}} = \hat{f}^{\delta} - \hat{f}^{\delta \mathrm{D}}$ is defined, which takes the jump value at the cell interface:

$$\hat{f}^{\delta \mathrm{C}}(-1) = \hat{f}_L^{\mathrm{com}} - \hat{f}_L^{\delta \mathrm{D}}, \tag{11}$$

$$\hat{f}^{\delta \mathrm{C}}(1) = \hat{f}_R^{\mathrm{com}} - \hat{f}_R^{\delta \mathrm{D}}. \tag{12}$$

Here, $\hat{f}_L^{\delta \mathrm{D}}$ and $\hat{f}_R^{\delta \mathrm{D}}$ are the values of the discontinuous function $\hat{f}^{\delta \mathrm{D}}$ taken at the left and right interfaces of the current element, and $\hat{f}_L^{\mathrm{com}}$ and $\hat{f}_R^{\mathrm{com}}$ are the numerical fluxes at the left and right interfaces. In order to calculate the numerical flux, values of the approximate solution $\hat{u}^{\delta}$ at both sides of an interface are obtained using Eq. (8), and then a suitable numerical flux solver is applied. In this study, the local Lax-Friedrichs flux (Rusanov flux) is used.

Now, we can define two correction functions, $g_L(r)$ and $g_R(r)$, that correspond to the left and right interfaces of the current element to introduce the correction to the discontinuous flux function. To meet the aforementioned requirements for the continuous flux function $\hat{f}^{\delta}$, $g_L(r)$ and $g_R(r)$ should be a polynomial of degree $K+1$ in the current element that approximate zero in some sense, satisfy the boundary conditions at the left and right interfaces,

$$g_L(-1) = 1,\ g_L(1) = 0, \tag{13}$$

$$g_R(-1) = 0,\ g_R(1) = 1, \tag{14}$$

and the symmetry,

$$g_L(r) = g_R(-r). \tag{15}$$

Thus, the correction flux $\hat{f}^{\delta \mathrm{C}}$ can be written in terms of $g_L$ and $g_R$ as

$$\hat{f}^{\delta \mathrm{C}} = \left(\hat{f}_L^{\mathrm{com}} - \hat{f}_L^{\delta \mathrm{D}}\right) g_L(r) + \left(\hat{f}_R^{\mathrm{com}} - \hat{f}_R^{\delta \mathrm{D}}\right) g_R(r). \tag{16}$$

The continuous flux function is constructed by $\hat{f}^{\delta} = \hat{f}^{\delta \mathrm{D}} + \hat{f}^{\delta \mathrm{C}}$, and its divergence at each solution point $r_j$ is defined by

$$\frac{\partial \hat{f}^{\delta}}{\partial r}(r_j) = \sum_{k=0}^{K} \hat{f}_j^{\delta} \frac{\mathrm{d}l_k}{\mathrm{d}r}(r_j) + \left(\hat{f}_L^{\mathrm{com}} - \hat{f}_L^{\delta \mathrm{D}}\right) \frac{\mathrm{d}g_L}{\mathrm{d}r}(r_j) + \left(\hat{f}_R^{\mathrm{com}} - \hat{f}_R^{\delta \mathrm{D}}\right) \frac{\mathrm{d}g_R}{\mathrm{d}r}(r_j). \tag{17}$$

Finally, the semi-discrete expression of Eq. (5) for each solution point is

$$\frac{\mathrm{d}\hat{u}_j^{\delta}}{\mathrm{d}t} = -\frac{\partial \hat{f}^{\delta}}{\partial r}(r_j). \tag{18}$$

### 2.2 VCJH (Vincent-Castonguay-Jameson-Huynh) Correction Function

As shown in [7], the conservative property of a FR scheme is independent of the correction function, but different FR schemes are characterized by different choices of the correction function and solution point. For 1D linear scalar conservation laws, Vincent et al. [15, 20] devised a class of 1D VCJH correction functions $g_L$ and $g_R$ leading to energy stable FR schemes having $(2K-1)$th order of super-accuracy with $K+1$ solution points, which are one-parameter correction functions as follows,

$$g_L = \frac{(-1)^K}{2}\left[L_K - \left(\frac{\eta L_{K-1} + L_{K+1}}{1+\eta}\right)\right], \tag{19}$$

$$g_R = \frac{1}{2}\left[L_K + \left(\frac{\eta L_{K-1} + L_{K+1}}{1+\eta}\right)\right], \tag{20}$$

where $L_K$ is a Legendre polynomial of degree $K$, and $\eta$ is a free scalar parameter that must lie within the range

$$-1 < \eta < \infty. \tag{21}$$

The choice of $\eta$ has influence on dispersion-dissipation properties, accuracy order, and CFL limit [45]. Setting $\eta = 0$, a collocation nodal DG scheme is recovered, and a few other schemes can be recovered with different choices of $\eta$ [15].

For a linear flux function, the energy stable property of the VCJH FR scheme holds for an arbitrary choice of solution points. However, if the flux function is nonlinear as in the Euler equations, the locations of solution points have a significant impact on the nonlinear stability because the collocation projection employed to construct $\hat{f}^{\delta \mathrm{D}}$ will introduce aliasing errors [46]. In this paper, the solution points are chosen to be Gauss-Legendre nodes as [47] recommended, which could minimize the aliasing errors, and $\eta = 0$ is adopted.

## 3 *a Posteriori* Subcell Limiting Process

In this study, we extend the a posteriori subcell finite volume limiter for the DG method [40] to the FR scheme. Though called limiter, this limiting process can be viewed as the h-p adaption [18] in the sense that the marked cells are divided into many smaller subcells, and then a robust low order finite volume scheme is used to recalculate the subcell mean values. In this way, we may fully exploit the subcell resolution capability of the FR scheme and capture sharp shocks inside a cell.

In the a posteriori subcell FV limiter, the physical admissibility and numerical admissibility criteria are used to detect troubled cells in the unlimited candidate FR solution at the new time $t^{n+1}$. If the candidate solution is considered to be unacceptable, the solution at the previous time $t^n$ in troubled cells and their face-neighbouring cells is distributed to corresponding subcell mean values, and then a robust finite volume method is used to carry out the evolution of these subcell means. Finally, the subcell mean values are reconstructed to yield the FR solution in troubled cells. Unlike [40, 42], the present numerical admissibility detection uses a KXRCF shock detector [44] before the relaxed discrete maximum principle detection. This modification can alleviate numerical wiggles caused by frequent switches between "good" and "troubled" cells near strong shocks, and improve the computational efficiency.

### 3.1 Subcell Data Projection and Reconstruction

To carry out limiting process with the FV subcell limiter, the FR solution $\hat{u}^\delta$ needs to be projected onto a set of subcell averages $\hat{v}_m^\delta$ in the same troubled cell. Divide $\hat{\Omega}$ of a troubled cell into $(M+1)$ subcells $S_m$, $m = 0, \ldots, M$: $\hat{\Omega} = \bigcup_m S_m$, which is an equidistant non-overlapping subgrid partition of the reference element. Figure 1 gives a typical partition of the element with five solution points into $(4+1)$ subcells. Subcell mean values $\hat{v}_m^\delta$, $m = 0, \ldots, M$, are defined by

$$\hat{v}_m^\delta = \frac{1}{|S_m|}\int_{S_m} \hat{u}^\delta(r)\mathrm{d}r. \tag{22}$$

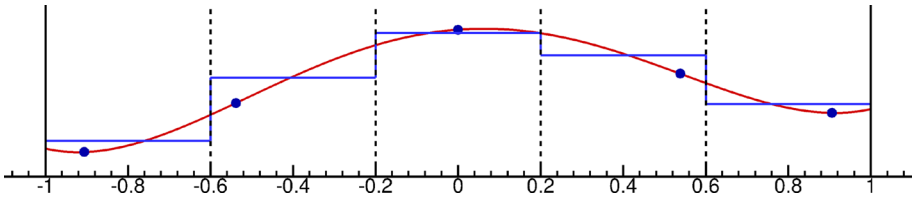


**Fig. 1** Diagram of subcells on a reference element for the case $M = K = 4$. The blue circle are solution points which are chosen to be Gauss-Legendre points in this paper. The red curve is the interpolation polynomial of FR solution (8). The vertical lines are boundaries of subcells, and the blue solid horizontal segments denote subcell mean values of the interpolation polynomial of solution (Color figure online)

Indeed, by defining a *projection operator* $\mathcal{P}$ (matrix) on the reference element $\hat{\Omega}$ using the Lagrange polynomial (9) as

$$\mathcal{P}_{m,j} = \frac{1}{|S_m|}\int_{S_m} l_j(r)\mathrm{d}r, \tag{23}$$

Eq. (22) can be written as

$$\begin{pmatrix} \hat{v}_0^\delta \\ \vdots \\ \hat{v}_M^\delta \end{pmatrix} = \mathcal{P}\begin{pmatrix} \hat{u}_0^\delta \\ \vdots \\ \hat{u}_K^\delta \end{pmatrix}. \tag{24}$$

To gather the piecewise subcell mean values back into a high order FR polynomial, the *reconstruction operator* $\mathcal{R}$ is applied: find a polynomial $\hat{u}^\delta(r)$ of degree $K$ such that

$$\frac{1}{|S_m|}\int_{S_m} \hat{u}^\delta(r)\mathrm{d}r = \hat{v}_m^\delta, \quad m = 0, \ldots, M. \tag{25}$$

This is a classical reconstruction problem of a high order polynomial from given cell averages arising in FV methods [48].

In general cases, the number of subcells in the reconstruction can be more than the number of unknowns in the reconstructed polynomial [40], so $\hat{u}^\delta(r)$ is reconstructed by a weighted least-squares reconstruction procedure [49], or a constrained least-squares reconstruction procedure [40, 41].

For 1D cases in this paper, the number of subcells is equal to the number of solution points, i.e. $M + 1 = K + 1$. Under this setup, $\mathcal{P}$ is a non-singular square matrix, the reconstruction operator $\mathcal{R}$ is nothing but the inverse matrix of $\mathcal{P}$, and the reconstruction Eq. (25) holds exactly rather than in the least-squares sense. This can exactly keep the conservation between the subcell averages $\hat{v}_m$ and the FR solution mean $\bar{u}_i$ on the corresponding cell $i$ [42].

### 3.2 Troubled Cell Detector

Once the candidate solution $\hat{u}_{i,j}^{*,n+1}$ for all solution points $j$ in all cells $i$ at the new time $t^{n+1}$ has been computed by the unlimited FR method, the troubled cell detection is carried out to decide whether the candidate solution is admissible. As in [40–42], we use two criteria for the detection, one addressing the physical admissibility detection (PAD) like negative density and pressure, another addressing the numerical admissibility detection (NAD) like spurious oscillations.

The PAD proceeds as follows:

- Check if the candidate solution lies in a physical admissible set (positivity of the pressure and density for compressible fluid flow equations, $\cdots$),
- Check if there is any `NaN` value.

These are the minimum requirements for a robust scheme. To tackle spurious oscillations, we use the Discrete Maximum Principle in the sense of mean value [38] which states that the FR solution on the main cell at the time $t^{n+1}$ should lie in the bounds of mean values of solution on the main cell $i$ and its direct neighbor cells ($i-1$ and $i+1$) at the previous time $t^n$. To maintain a high order accuracy near smooth extrema, the DMP is relaxed to yield the following NAD criterion [39, 40, 42].

The NAD proceeds as follows:

- Check if the following relaxed DMP is satisfied,

$$\min(\bar{u}_{i-1}^n, \bar{u}_i^n, \bar{u}_{i+1}^n) - \delta_i \le \hat{u}_{i,j}^{*,n+1} \le \max(\bar{u}_{i-1}^n, \bar{u}_i^n, \bar{u}_{i+1}^n) + \delta_i \tag{26}$$

  for $j = 0, \cdots, K$.

We remark that if the DMP is implemented in a strict way, i.e., $\delta_i = 0$ in (26), then cells in constant regions may be misjudged as troubled cells due to roundoff errors. Furthermore, the upper and lower bounds of the mean values are stricter than the continuous function bounds, making the scheme dissipative and at most $O(\Delta x_i^2)$ accurate [39]. The small quantity $\delta_i$ in (26) for relaxing the DMP will admit small numerical oscillations but can avoid problems with roundoff errors and guarantee a high order accuracy at smooth extrema. In this paper, we adopt

$$\delta_i = \max\left(\delta_0, \epsilon \cdot \left(\max(\bar{u}_{i-1}^n, \bar{u}_i^n, \bar{u}_{i+1}^n) - \min(\bar{u}_{i-1}^n, \bar{u}_i^n, \bar{u}_{i+1}^n)\right)\right), \tag{27}$$

where we set $\delta_0 = 10^{-4}$ and $\epsilon = 10^{-3}$ as Dumbser et al. [40] used.

In our experience, we find that the cell mean value-based relaxed DMP detection (26) can address the issue of spurious oscillations for polynomial degrees 2 and 3 (denote by P2, P3) FR methods. However, it will miss out spurious oscillations within a cell and does not work well for P4 above FR methods. Thus for P4 above FR schemes we will use the subcell numerical admissibility detection (SubNAD) to detect numerical oscillations in place of the main cell level NAD (26). The subcell NAD is similar to that in [42].

The SubNAD proceeds as follows:

- Check if the following relaxed DMP is satisfied at the subcell level,

$$\min\left(\hat{v}_{i,j-1}^n, \hat{v}_{i,j}^n, \hat{v}_{i,j+1}^n\right) - \delta_{i,j} \le \hat{v}_{i,j}^{*,n+1} \le \max\left(\hat{v}_{i,j-1}^n, \hat{v}_{i,j}^n, \hat{v}_{i,j+1}^n\right) + \delta_{i,j}, \tag{28}$$

  for $j = 0, \ldots, K$, where

$$\delta_{i,j} = \max\left(\delta_0, \epsilon\left(\max\left(\hat{v}_{i,j-1}^n, \hat{v}_{i,j}^n, \hat{v}_{i,j+1}^n\right) - \min(\hat{v}_{i,j-1}^n, \hat{v}_{i,j}^n, \hat{v}_{i,j+1}^n)\right)\right). \tag{29}$$

Here, we set $\hat{v}_{i,-1}^n = \hat{v}_{i-1,K}^n$ and $\hat{v}_{i,K+1}^n = \hat{v}_{i+1,0}^n$. If any subcell of the main cell $i$ violates the SubNAD (28), the main cell $i$ will be marked as troubled.

It should be mentioned that the a posteriori limiter compares the solutions at two different times, i.e., compare $\hat{u}^{*,n+1}$ with bounds of $\hat{u}^n$, rather than comparing solutions at the same time level as in *a priori* limiter. In fact, the a posteriori way is a rather straightforward implementation of the continuous maximum principle which states that the solution at any time will be bounded by the maximum and minimum value of the initial values.

The aforementioned PAD-NAD procedure generally works well for unsteady problems. However, we have found that the NAD using only the relaxed DMP does not work well for steady detonation problems. The reason could be explained as follows. The data transformation (24)–(25) between the FR and subcell FV solutions in a troubled cell near a shock will cause the Runge phenomenon [50], which generates numerical perturbations larger than the steady state convergence tolerance. After the diffusive subcell limiting, the troubled cell may not be marked as troubled in several time steps until numerical oscillations have grown sufficiently large to violate the relaxed DMP (26) or (28) again. Thus, the computation in these cells will switch between the FR and subcell FV schemes frequently. In general, this is not a big issue for unsteady problems, however, it will introduce numerical perturbations that prevent the maximum pressure history from converging to a tolerance like $10^{-4}$ for the simulation of steady detonation. In order to mark the troubled cells in the vicinity of steady detonation waves successively, the KXRCF shock detector [44] is introduced into the NAD procedure to form the present modification, which is described in Sect. 3.3.

### 3.3 NAD Incorporated with the KXRCF Shock Detector

Denote the cell interface vales of a cell $i$ by $\hat{u}^n_{i,L}$ and $\hat{u}^n_{i,R}$, which are calculated using the Lagrange interpolation. In a way similar to the KXRCF shock detector [44], we define the boundary jump associated with the cell $i$ as

$$I_i = \max\left(|\,\hat{u}^n_{i,L} - \hat{u}^n_{i-1,R}\,|,\ \ |\,\hat{u}^n_{i,R} - \hat{u}^n_{i+1,L}\,|\right). \tag{30}$$

For a $(K+1)$th order accurate scheme, the following result holds [44]:

$$I_i = \begin{cases} \mathcal{O}(h^{K+1}), & \text{if } \Omega_i, \Omega_{i\pm1} \text{ are smooth regions of solution,} \\ \mathcal{O}(1), & \text{if any of } \Omega_i, \Omega_{i\pm1} \text{ contains discontinuities.} \end{cases} \tag{31}$$

Here, $h = x_{i+1/2} - x_{i-1/2}$ is the mesh size. Now, we can construct a discontinuity detector by normalizing $I_i$ with the product of the cell-averaged solution $\bar{u}^n_i$ and an "averaged" convergence rate $\mathcal{O}(h^{\frac{K+1}{2}})$:

$$I^*_i = \frac{I_i}{h^{\frac{K+1}{2}}\bar{u}^n_i}. \tag{32}$$

We see that if $h \to 0$, then $I^*_i \to 0$ in smooth regions and $I^*_i \to \infty$ near discontinuities [44]. Therefore, we will mark the cell as discontinuous (troubled) if $I^*_i$ is larger than a specified value $C_D$. In fact, the above asymptotic behavior also allows us to mark smooth regions if $I^*_i$ is smaller than another specified small threshold value $C_S < C_D$. So, we let the smooth and discontinuous cells detected by the KXRCF detector bypass the detection (26) or (28), leaving only the intermediate cells ($C_S \le I^*_i \le C_D$) for the detection (26) or (28).

Summarizing the discussions above, the Smooth and Shock region Detection (SSD) using the KXRCF detector is combined with the previous NAD or subcell NAD so as to form our modified NAD or subNAD as follows:

- Compute $I^*_i$.
- Directly mark the cell as acceptable if $I^*_i < C_S$.

- Directly mark the cell as troubled if $I_i^* > C_D$.
- Carry out NAD (26) or SubNAD (28) if $C_S \le I_i^* \le C_D$.

In this paper, we take $C_S = 10^{-3}$ and $C_D = 1.0$ for all the numerical examples.

### 3.4 Subcell Limiting Process

After the detection phase by PAD and NAD, a robust finite volume method is used to recompute the subcell mean values in troubled cells and then these mean values are assembled to the final FR solution. Here, a subcell finite volume scheme is abbreviated as

$$\hat{v}^{\delta,n+1} = \mathcal{A}(\hat{v}^{\delta,n}). \tag{33}$$

Obviously, the first order Godunov scheme [51] can be used for (33). However, it is too dissipative. As an option, a second order Godunov type FV scheme using the MUSCL reconstruction [52] with the minmod limiter [53] for characteristic variables is used.

Similar to the marking strategy in [40, 42], if a cell is detected as troubled, its left and right neighbor cells are also marked as troubled. This extra marking is useful for improving the quality of numerical solution.

### 3.5 Summary of the a posteriori Subcell Limiter

**Algorithm 1** Procedure for the a posteriori subcell finite volume limiter

```
Carry out unlimited FR solver
for i = 1 to N_elem do
    if PAD violated then
        mark_{i-1} = mark_i = mark_{i+1} = 1
        continue
    end if
    if I_i^* ≥ C_S then
        if I_i^* > C_D then
            mark_{i-1} = mark_i = mark_{i+1} = 1
        else if NAD or SubNAD violated then
            mark_{i-1} = mark_i = mark_{i+1} = 1
        end if
    end if
end for
for i = 1 to N_elem do
    if mark_i == 1 then
        Projection: v̂_i^n = P(û_i^n)
        Subcell Finite Volume Solver: v̂_i^{n+1} = A(v̂_i^n)
        Reconstruction: û_i^{n+1} = R(v̂_i^{n+1})
    end if
end for
```

Let us summarize Sects. 3.1, 3.2 and 3.4 in Algorithm 1, which computes the FR solution at the time $t^{n+1}$ from the FR solution at the time $t^n$.

## 4 Governing Equations and Initial Conditions for 1D Detonations

### 4.1 Governing Equations

The governing equations used in this work for modeling 1D detonation problems are the 1D reactive Euler equations for the gas mixture with two species-the reactant and the product:

$$\begin{aligned}
&\frac{\partial \rho}{\partial t}+\frac{\partial(\rho u)}{\partial x}=0,\\
&\frac{\partial(\rho u)}{\partial t}+\frac{\partial(\rho u^2+p)}{\partial x}=0,\\
&\frac{\partial E}{\partial t}+\frac{\partial\left(u(E+p)\right)}{\partial x}=0,\\
&\frac{\partial(\rho Y)}{\partial t}+\frac{\partial(\rho u Y)}{\partial x}=\dot{\omega},
\end{aligned} \tag{34}$$

where $\rho$ is the density, $p$ is the pressure, $u$ is the velocity, $E$ is the specific total energy, and $0 \leq Y \leq 1$ is the mass fraction of the reactant, which equals one when the single-step irreversible chemical reaction has not started, and zero when the reaction has completed.

The chemical reaction releases heat to sustain the propagation of detonation wave. The reaction heat is accounted for in the total energy as

$$E=\frac{p}{\gamma-1}+\frac{1}{2}\rho u^2+\rho Y q_0, \tag{35}$$

where $q_0$ is the heat release due to the chemical reaction, and $\gamma$ is the ratio of specific heats. The mass production rate of the reactant, $\dot{\omega}$, is given by the Arrhenius rate law

$$\dot{\omega}=-A\rho Y e^{-E_a/T}. \tag{36}$$

Here, $A$ is the pre-exponential factor and $E_a$ is the activation energy. The temperature $T$ is determined by the ideal gas EOS

$$T=\frac{p}{\rho R}. \tag{37}$$

where $R$ is the specific gas constant. Following the normalization way [5, 54], we set $R=1$ in this study.

### 4.2 Initial Conditions

The setup of the initial conditions for solving Eq. (34) is given by the approximate solution of the classical 1D steady ZND solution. For completeness, the derivation in [55, 56] will be given below to provide a brief review.

Assume that the detonation wave propagates at a constant velocity $D$ in a quiescent unburned gas in the $x$ direction. Transform the coordinate $x$ in Eq. (34) to a new one such that the origin is moving with the constant velocity $D$. Then, Eq. (34) can be transformed into the steady equations in the new coordinate still denoted as $x$,

$$\frac{\mathrm{d}(\rho u)}{\mathrm{d}x}=0, \tag{38a}$$

$$\frac{\mathrm{d}(\rho u^2+p)}{\mathrm{d}x}=0, \tag{38b}$$

$$\frac{\mathrm{d}\left(u(\rho E+p)\right)}{\mathrm{d}x}=0, \tag{38c}$$

$$\frac{\mathrm{d}(\rho u Y)}{\mathrm{d}x}=\dot{\omega}. \tag{38d}$$

The non-dimensional flow variables in the unburned zone in the new system are given by

$$\rho=1,\ p=1,\ T=1,\ u=-D,\ Y=1. \tag{39}$$

Integrating Eqs. (38a), (38b) and (38c) from the unburned zone with the state (39) to any point in the flame zone, one obtains the following relations,

$$\rho u=-D, \tag{40}$$

$$\rho u^2+p=D^2+1, \tag{41}$$

$$\rho u\left(\frac{\gamma}{\gamma-1}\frac{p}{\rho}-q_0\lambda+\frac{1}{2}u^2\right)=-D\left(\frac{\gamma}{\gamma-1}+\frac{1}{2}D^2\right), \tag{42}$$

where $\lambda=1-Y$ is the mass fraction of the product. Eqs. (40) and (41) can be rewritten as

$$\rho=-D/u, \tag{43}$$

$$p=Du+D^2+1. \tag{44}$$

By inserting Eqs. (43) and (44) into Eq. (42), one obtains

$$\frac{1}{2}u^2+\frac{\gamma}{\gamma+1}\left(D+\frac{1}{D}\right)u+\frac{\gamma-1}{\gamma+1}\left(q_0\lambda+\frac{\gamma}{\gamma-1}+\frac{1}{2}D^2\right)=0. \tag{45}$$

This is a second order polynomial equation about $u$ and its solution has two roots as follows,

$$u_{\pm}=-\frac{\gamma}{\gamma+1}\left(D+\frac{1}{D}\right)\pm\sqrt{\xi(\lambda)}, \tag{46}$$

where

$$\xi(\lambda)=\left[\frac{\gamma}{\gamma+1}\left(D+\frac{1}{D}\right)\right]^2-2\frac{\gamma-1}{\gamma+1}\left(q_0\lambda+\frac{\gamma}{\gamma-1}+\frac{1}{2}D^2\right). \tag{47}$$

Note that the root $u_-$ in Eq. (46) does not exist in real situations. The Chapman-Jouguet (CJ) velocity follows from Eq. (47) by setting $\xi\ |_{\lambda=1}=0$,

$$D_{\mathrm{CJ}}^2=[\gamma+(\gamma^2-1)q_0]+\sqrt{[\gamma+(\gamma^2-1)q_0]^2-\gamma^2}. \tag{48}$$

Define the overdriven factor $f$ as

$$f=\frac{D^2}{D_{\mathrm{CJ}}^2}. \tag{49}$$

Given the parameters $\gamma$ and $q_0$, $D_{\mathrm{CJ}}$ is determined by Eq. (48), then by specifying a value of $f$, the detonation velocity $D$ is determined by Eq. (49). And then $u$, $p$, $\rho$ and $T$ can be got from Eqs. (46), (44), (43) and (37), respectively, for a value of $\lambda$ (or $Y$).

Finally, by substituting Eqs. (36) and (40) into Eq. (38d), one obtains an ordinary differential equation for $Y$

$$\frac{\mathrm{d}Y}{\mathrm{d}x}=\frac{A\rho(Y)Y}{D}e^{-E_a/T(Y)}, \tag{50}$$

which can be integrated in $x$ to obtain the profile $Y(x)$ by using standard numerical methods like Runge–Kutta methods [5, 54] if $A$, $E_a$ and a starting point for the integration are given.

The half length of the reaction zone, $L_{1/2}$, is defined as the distance between the detonation head point where $Y = 1$ and the point in the reaction zone where half of the reactant is consumed by combustion ($Y = 0.5$). By integrating Eq. (50), the half reaction length is defined as

$$L_{1/2} = \frac{D}{A}\int_{1/2}^{1} \frac{\mathrm{d}Y}{\rho(Y)Y\exp\left(-E_a/T(Y)\right)}. \tag{51}$$

Equation (51) implies that $L_{1/2}$ is related to $A$ with given $(\gamma, q_0, f, E_a)$. For convenience, we will fix $L_{1/2} = 1$ across different configurations of $(\gamma, q_0, f, E_a)$ by choosing the corresponding pre-exponential factor $A$ according to Eq. (51), i.e.

$$A = D\int_{1/2}^{1} \frac{\mathrm{d}Y}{\rho(Y)Y\exp\left(-E_a/T(Y)\right)}. \tag{52}$$

In this study, following Hu [3], instead of integrating Eq. (50) to get $Y(x)$, a simple stepwise approximation is adopted for the initial $Y$ profile as given by

$$Y(x) = \begin{cases} 0, & x \le x_0 - L_{1/2}, \\ \dfrac{1}{2}\left[\tanh\left(\pi\dfrac{x - x_0}{L_{1/2}}\right) + 1\right], & x_0 - L_{1/2} < x \le x_0 + L_{1/2}, \\ 1, & x > x_0 + L_{1/2}, \end{cases} \tag{53}$$

where $x_0 = 1$ is chosen to be the center of the reaction zone, and $L_{1/2} = 1$.

To sum up, the present initial conditions are set up as follows. Given values of $\gamma$, $q_0$ and $f$, $D$ is calculated by Eqs. (48) and (49). Then, given $E_a$, $A$ is calculated from (52). The simple initial distribution $Y(x)$ is given by Eq. (53), and then $u(x)$, $\rho(x)$, $p(x)$ and $T(x)$ in the computational domain can be determined from Eqs. (46), (44), (43) and (37), respectively.

Remembering that, with (52), the pre-exponential factor $A$ is determined from the given $(\gamma, q_0, f, E_a)$ under the assumption $L_{1/2} = 1$. However, for convenience of computing the chemical reaction rate (36), both the given $(\gamma, q_0, f, E_a)$ and the calculated $A$ will be used to prescribe detonation conditions. A typical ZND wave solution with the parameters $x_0 = 1$, $\gamma = 1.2$, $q_0 = 50$, $E_a = 50$, $f = 1.8$ ($A = 145.69$) is shown in Fig. 2.

## 5 Numerical Examples

In this section, a series of test cases are used to demonstrate the performance of the VCJH FR scheme in conjunction with the proposed limiting algorithm. The local Lax-Friedrichs numerical flux is used for the FR and subcell FV schemes. The third-order SSP Runge–Kutta method [57] is used for the time integration of the semi-discretized scalar Eq. (18) and Euler equations [5, 54]. Because the present detonation simulation is focused on the maximum pressure history, we use the pressure as the detection variable in the NAD and SubNAD.

In the followings, a FR method with the subcell limiter is denoted as "FR$K$-`Limiter`" scheme, where $K$ represents a degree-$K$ polynomial ($K + 1$ order accurate) approximation for the solution in a cell, and `Limiter` takes either "God" (first order Godunov FV method) or "TVD" (second order TVD FV method). For example, "FR2-TVD" denotes the 3rd-order accurate FR method in conjunction with the second order TVD method for subcell mean values. For $K = 2, 3$, NAD (26) is used while for $K \ge 4$, SubNAD (28) is used. The CFL number is chosen to be $1/(2K + 1)$ for all the numerical examples.

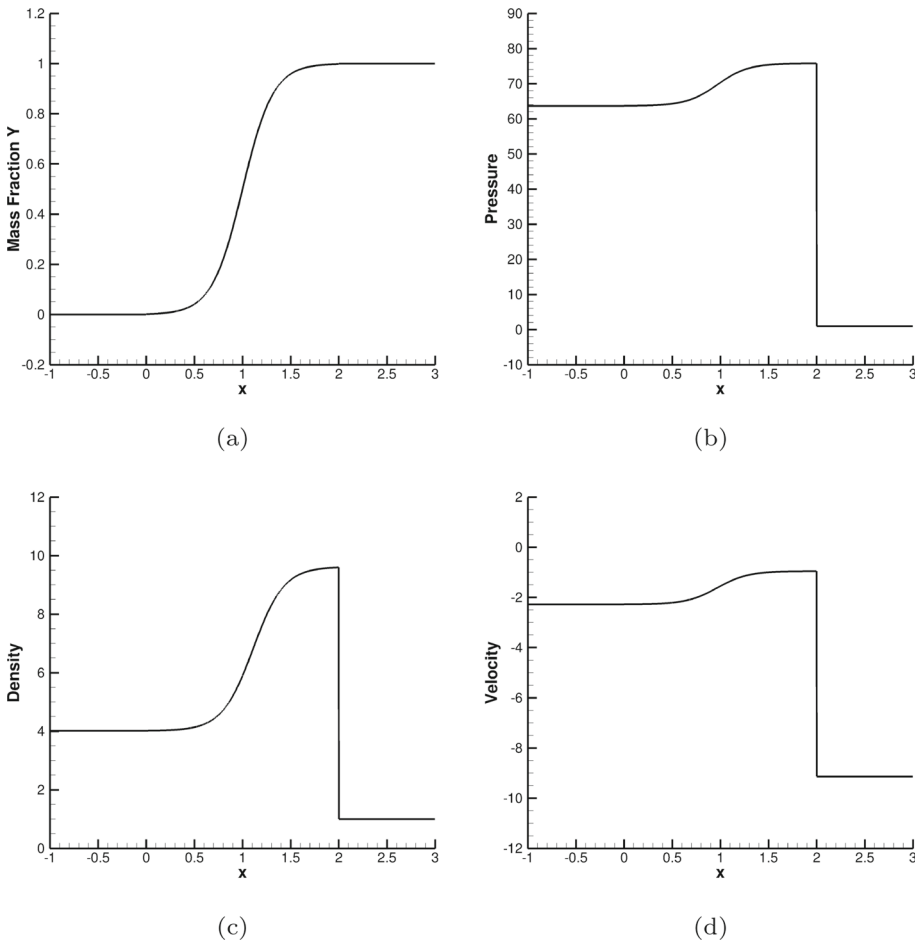


**Fig. 2** Initial profiles of **a** mass fraction, **b** pressure, **c** density, **d** velocity using an one-dimensional ZND detonation wave

In the numerical tests in Sects. 5.2, 5.3 and 5.4 we solve the traditional Euler equations for an ideal gas with $\gamma = 1.4$. For the detonation tests from Sect. 5.5 on, we solve the reactive Euler Eq. (34) with fixed $\gamma = 1.2$, $q_0 = 50$, $E_a = 50$ and the initial conditions in Sect. 4.2. And different detonation tests will be characterized by different values of $f = 1.3 \sim 1.8$ together with the calculated pre-exponential factors $A$.

### 5.1 Numerical Convergence Test

To verify the accuracy of the FR scheme with the a posteriori subcell limiter, we use the 1D linear advection equation

$$\frac{\partial u}{\partial t} + \frac{\partial u}{\partial x} = 0 \tag{54}$$

**Table 1** $L^2$ and $L^\infty$ errors and convergence rates of the FR2-TVD scheme for the linear advection equation (54) with the initial condition (55)

| Scheme | $N_{\text{elem}}$ | $L^2$ error | Order | $L^\infty$ error | Order |
|---|---|---|---|---|---|
| FR2-TVD | 40 | 1.14011E−05 | | 1.79643E−05 | |
| | 80 | 1.42245E−06 | 3.00272 | 2.24099E−06 | 3.00293 |
| | 160 | 1.77745E−07 | 3.00050 | 2.79853E−07 | 3.00139 |
| | 320 | 2.22177E−08 | 3.00003 | 3.49659E−08 | 3.00065 |
| | 640 | 2.77739E−09 | 2.99990 | 4.36960E−09 | 3.00038 |
| | 1280 | 3.47388E−10 | 2.99911 | 5.45986E−10 | 3.00056 |

with periodic boundary conditions on two ends of the computational domain $x \in [0, 1]$. The initial condition is a shifted sine wave,

$$u(x, 0) = 0.99 \sin(2\pi x) + 1.0. \tag{55}$$

Since we use the third-order SSP Runge–Kutta method for the time integration, the time step is take as $\Delta t = \text{CFL} \cdot \Delta x^{(K+1)/3}$ so that the temporal accuracy is commensurate with the spatial one. We compute the solution for one period, i.e., time $t = 1$ as in [36]. The errors and rates of convergence computed by the FR2-TVD scheme are shown in Table 1. We see that the scheme has achieved the theoretical third order of convergence. The results by the FR2-God scheme (not shown here) are the same because there are no detected troubled cells and thus no limiting.

### 5.2 Sod's Shock Tube Problem

The Sod shock tube problem [58] describes the 1D inviscid flow initiated by two states separated by an interface located at $x = 0.5$. The left state is a high pressure gas and the right state is a low pressure gas as given by

$$(\rho, u, p) = \begin{cases} (1, 0, 1), & 0 \le x \le 0.5, \\ (0.125, 0, 0.1), & 0.5 < x \le 1. \end{cases} \tag{56}$$

The computational domain is discretized with 100 cells, the simulation is carried out up to $t = 0.2$, and CFL number is set to 0.2. The reference solution is obtained using the exact Riemann solver [48]. Figure 3a shows the density profiles computed by the FR2-God and FR2-TVD schemes. It can be seen that both schemes do not generate spurious oscillations at the shock, and the FR2-TVD scheme has a better resolution for the contact discontinuity than the FR2-God scheme. Figure 3b shows the detected troubled cell history in time for the FR2-TVD scheme, in which the symbol "□" is used to represent the troubled cells and is plotted at the center of each troubled cell. It is seen that the detected troubled cells propagate always with the shock, but intermittently with the discontinuity and expansion waves. We have used the pressure as the detect variable, and thus there should not be detected troubled cells near the contact discontinuity all the time. But due to numerical undulations near the contact discontinuity (see Fig. 3a), the cells near the contact discontinuity are detected as troubled cells initially but are not detected as troubled cells between $t = 0.07$ and 0.14. To capture the contact discontinuity better the density may be a more suitable detect variable.

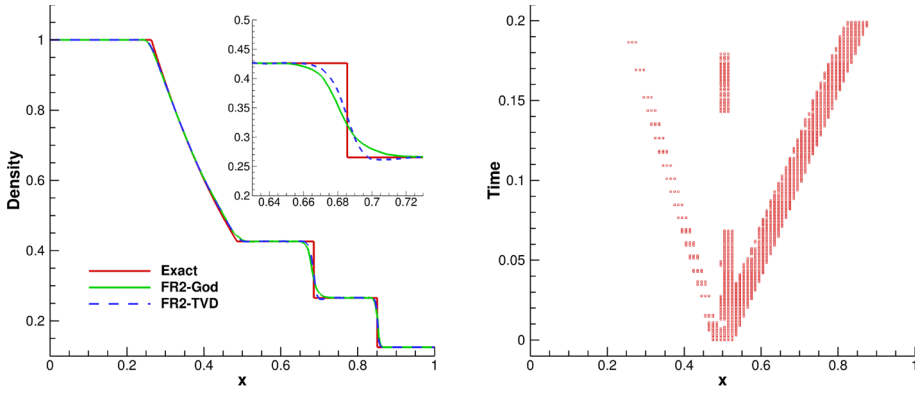


(a) Density profile (b) Troubled cell history

**Fig. 3** Density profiles at $t = 0.2$ computed by the FR2-God and FR2-TVD schemes **a** and troubled cell detection history by the FR2-TVD scheme **b** for the Sod shock tube problem on 100 cells with CFL = 0.2

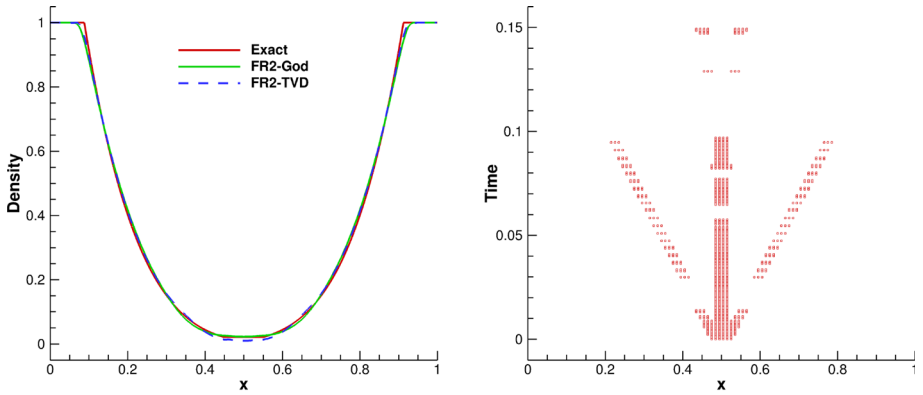


(a) Density (b) Troubled cell history

**Fig. 4** Density profiles at $t = 0.15$ computed by the FR2-God and FR2-TVD schemes **a** and trouble cell history detected by the FR2-TVD scheme **b** for the double expansion waves on 100 cells with CFL = 0.2

### 5.3 One-Dimensional Supersonic Expansion

This problem describes double rarefaction waves that move in opposite directions [59], which is often used to test the performance of a scheme near vacuum. The initial conditions are

$$(\rho, u, p) = \begin{cases} (1, -2, 0.4), & 0 \le x \le 0.5, \\ (1, 2, 0.4), & 0.5 < x \le 1. \end{cases} \tag{57}$$

The computational domain is discretized with 100 cells and the final time is $t = 0.15$. The CFL number used is 0.2. The FR2-God and FR2-TVD schemes are used. Figure 4a shows the computed density profiles. We see that the results contain no spurious oscillations and are in good agreement with the exact solution. Figure 4b shows the history of troubled cell mark. We see that the trouble cells can follow the movement of the two rarefaction heads

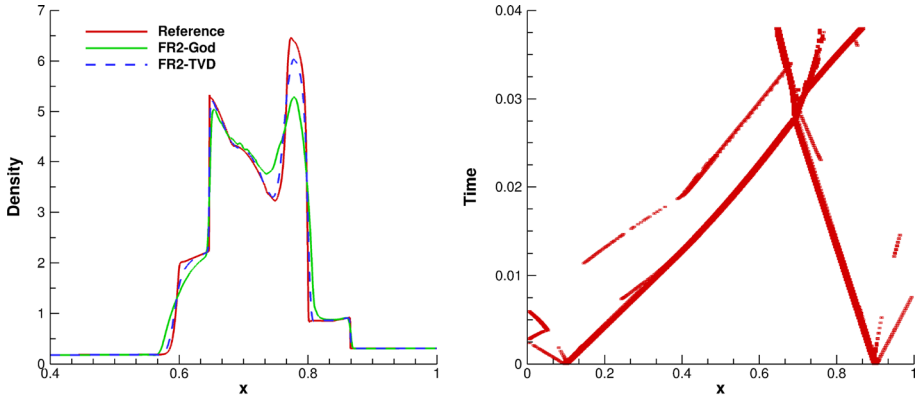


(a) Density (b) Troubled cell history

**Fig. 5** Density profiles at $t = 0.038$ computed by the FR2-God and FR2-TVD schemes **a** and trouble cell history detected by the FR2-TVD scheme **b** for the blast-wave problem on 400 cells with CFL = 0.2

and the central zone with low density and pressure. As the time goes on, the expansion heads become smooth, so the troubled cells disappear around the two heads.

### 5.4 Two Interacting Blast Waves

Now we consider the well-known interaction problem of two blast waves from Woodward and Colella [60]. The initial condition is

$$(\rho, u, p) = \begin{cases} (1, 0, 1000), & 0 \le x < 0.1, \\ (1, 0, 0.01), & 0.1 \le x < 0.9, \\ (1, 0, 100), & 0.9 \le x \le 1.0. \end{cases} \tag{58}$$

The computational domain is $x \in [0, 1]$. A reflecting boundary condition is applied at both ends. The grid has 400 uniform cells, the CFL number used is 0.2, and the output time is $t = 0.038$. Figure 5a shows the results computed by the FR2-God and FR2-TVD schemes where the solid line indicates the reference solution computed by a 2nd-order TVD finite volume method on 10000 grid cells. We see that both the FR2-God and FR2-TVD schemes can capture the basic interaction structures without numerical oscillations. However, we observe that the FR2-TVD scheme captures the structures with a higher resolution than the FR2-God scheme, especially near the contact discontinuities and the extremas. Figure 5b shows the time history of troubled cells. Again, since we us the pressure as the detection variable, troubled cells near contact waves are not constantly marked.

### 5.5 Stable Detonation Wave with $f = 1.8$

We now consider the numerical solution of the 1D reactive Euler Eq. (34) with the mass production rate (36).

According the linearized stability theory of the classical ZND wave, Bourlioux et al. [61] regarded the overdriven factor $f$ as a bifurcation parameter and the ZND profile becomes

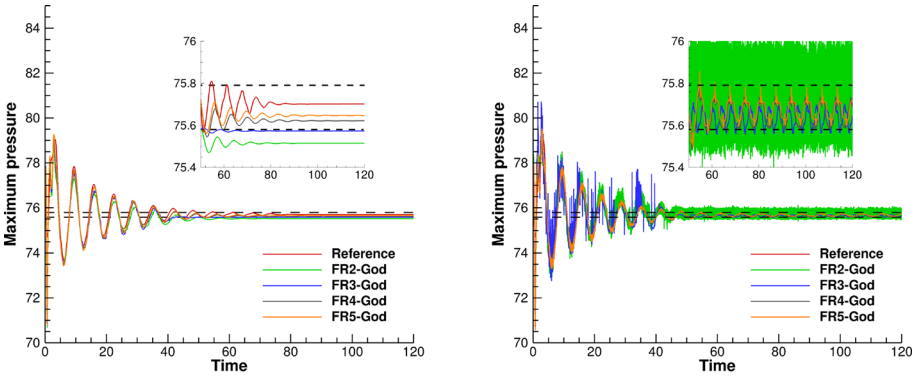


(a) NAD + SSD (b) NAD Only

**Fig. 6** Max pressure time history by various order FR schemes with the 1st-order Godunov FV subcell limiter for the stable detonation case with the overdriven factor $f = 1.8$ ($A = 145.69$). The small plot is an enlarged view. The horizontal lines are the ZND post shock pressure $p_{\text{ZND}} = 75.79$ and CJ Neumann point pressure $p_{\text{NP}} = 75.58$ respectively

more unstable as $f$ decreases. There is a critical value $f_c \approx 1.73$, above which the ZND profile is stable.

Denote the grid resolution with $N$ uniform cells lying in the half reaction length as resolution $\delta_N$. Since there is no exact solution for unsteady ZND problems, the numerical solution computed by the fifth order characteristic-wise reconstructed alternative WENO-JS finite volume scheme [5] with the local Lax-Friedrichs (Rusanov) numerical flux on the resolution $\delta_{160}$ under CFL $= 0.5$ is used as the reference solution in all the detonation examples.

We first simulate the stable detonation case with $f = 1.8$ ($A = 145.69$), $E_a = 50, q_0 = 50$ and $\gamma = 1.2$. The computational domain is $[-750, 50]$, and the boundary conditions are of Dirichlet type on both ends taking the ZND solution values with the assumed mass fraction distribution (53). The final time is $t = 120$. Since the initial data are not the exact solution of the ZND model, the simulation needs some time to compute a stable detonation solution that approximates the exact solution of the ZND model. In the early stage, the detonation front moves forth and back around $x = x_0 = 1$. As the simulation goes on, the numerical solution evolves into a steady state.

The peak pressure temporal history computed with the third to sixth order FR schemes on the resolution $\delta_{20}$ is shown in Figs. 6 and 7, in which we compare performance of the detectors with and without SSD. Two horizontal dashed lines are plotted as reference steady states, one is $p_{\text{NP}} = 75.58$ which is the pressure on the Neumann point [62] and another is $p_{\text{ZND}} = 75.79$ which is the exact post-shock pressure value of the ZND model [63]. From Figs. 6a and 7a we see that the numerical results by the FR schemes with SSD combined with either the 1st-order Godunov or 2nd-order TVD FV subcell limiter can converge to steady state. In contrast, Fig. 6b shows that the FR schemes without SSD fail to converge for the 1st-order Godunov subcell limiter as a result of improper tracing of the shock front. Figure 7b shows that the FR schemes with the 2nd-order TVD subcell limiter without SSD can converge, but at the cost of marking exceedingly more troubled cells than the counterpart with SSD (to be verified in Fig. 10b).

The pressure and density profiles computed with the FR2-God and FR2-TVD schemes on the resolution $\delta_{20}$ at time $t = 120$ are compared in Fig. 8. We can see that both results

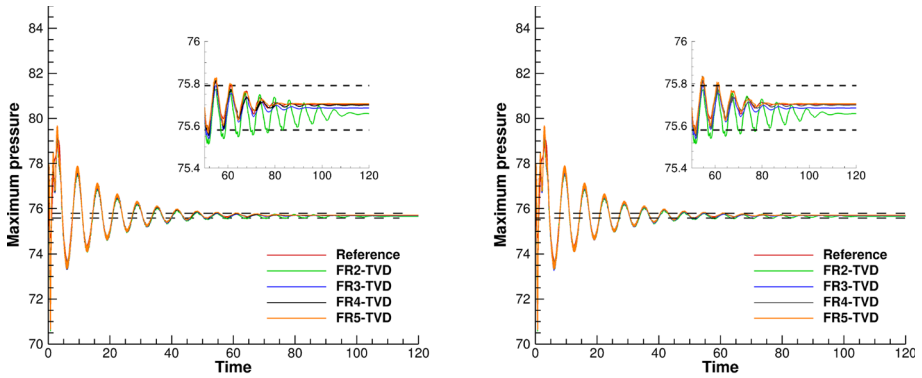


**Fig. 7** Max pressure time history for the detonation case $f = 1.8$ case computed by various order FR schemes with the 2nd-order TVD subcell FV limiter

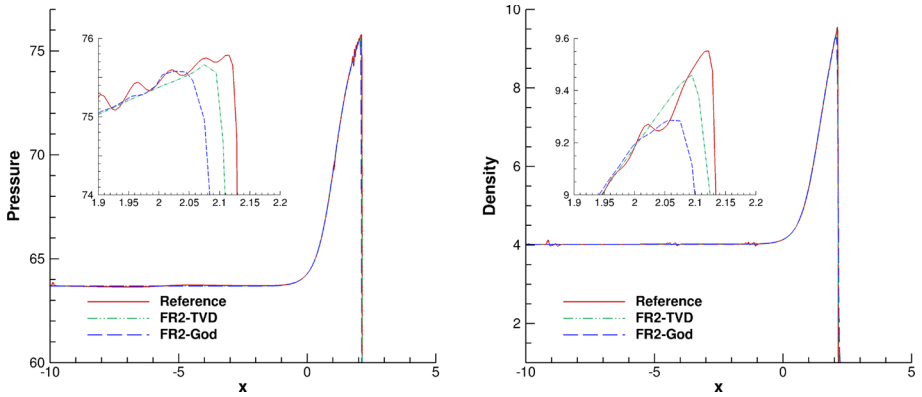


**Fig. 8** Pressure and density profiles computed with the FR2-TVD and FR2-God schemes for the case $f = 1.8$ at $t = 120$

are in good agreement with the reference solution. By comparison, the FR2-TVD scheme produces a shaper detonation front.

We compare the shock-resolving ability of the FR2-TVD, FR2-God, 5th-order WENO-JS and WENO-Z schemes under the same degrees of freedom (DOFs), i.e., $\delta_{20}$ for FR2 and $\delta_{60}$ for WENO-JS and WENO-Z. Figure 9 shows the pressure profile at $t = 120$. From Fig. 9b we can see that the shock resolution of the FR2-TVD scheme is close to those of the WENO-JS and WENO-Z schemes but the FR2-God scheme is more diffusive. However, Fig. 9a shows that the WENO-JS and WENO-Z schemes generate some non-physical oscillations near the end of the reaction zone and in the more left region, but the FR2-TVD and FR2-God schemes do not generate such fluctuations.

Figure 10a shows the troubled cell time history and the steady pressure profile at $t = 120$ computed by the FR2-TVD scheme. The time traces include all the identified troubled cells in the whole computational domain $[-750, 50]$. We see that the troubled cells are clustered around the detonation front, indicating that the present modified NAD can detect discontinuities accurately. By comparison, Fig. 10b shows the troubled cell history by the

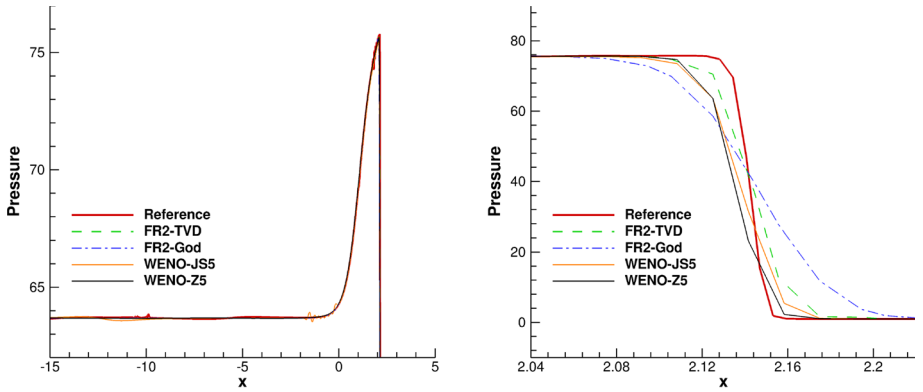


**Fig. 9** Comparison of pressure profiles by various schemes with same DOFs for the case $f = 1.8$ at $t = 120$. **a** View in $[-15, 5]$. **b** Zoom in $[2.04, 2.22]$

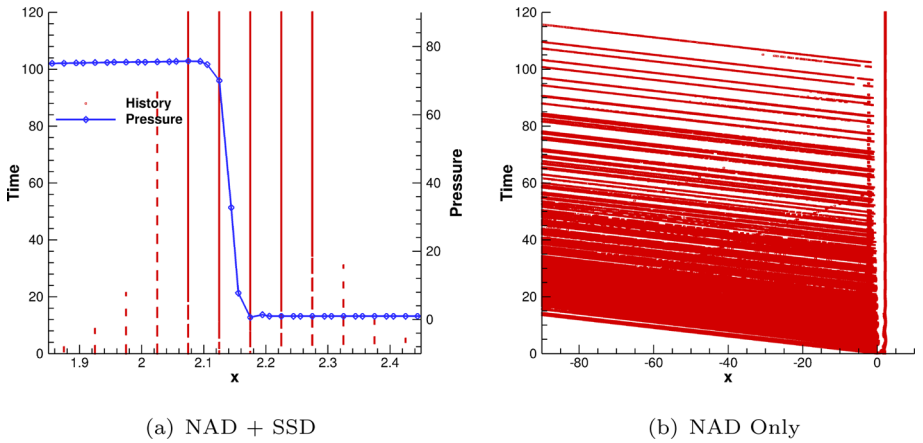


**Fig. 10** **a** Time history of troubled cells and the pressure profile at $t = 120$ computed by the FR2-TVD scheme with SSD on the resolution $\delta_{20}$ for the steady detonation case $f = 1.8$. Red circles are limiter use history plotted at the center of cells. The blue line with diamonds (solution points) is the pressure profile at $t = 120$. **b** Time history of troubled cells by the FR2-TVD scheme without SSD (Color figure online)

FR2-TVD scheme without SSD. It is seen that more troubled cells are unnecessarily marked in the left region of the detonation front. To compare the tracing efficiency, we show the number of detected troubled cells per time step averaged from the beginning of simulation to $t = 120$ in Table 2. The results illustrate that the combination of NAD and SSD can significantly reduce unnecessary marking, thus improving the computational efficiency.

### 5.6 Slightly Unstable Detonation Wave with $f = 1.6$

In this subsection, the detonation wave with the overdriven factor $f = 1.6$ ($A = 230.75$) and the same $(E_a, q_0, \gamma)$ values as in Sect. 5.5, is simulated with the resolution $\delta_{20}$ to the final time $t = 80$. The computational domain is still $[-750, 50]$. According to [61], the solution

**Table 2** Time averaged number of troubled cells from $t = 0$ to $t = 120$ for various order FR schemes on the resolution $\delta_{20}$ for the steady detonation case $f = 1.8$

| Detector | Limiter | FR2 | FR3 | FR4 | FR5 |
|---|---|---|---|---|---|
| NAD + SSD | God | 5.15 | 6.13 | 6.16 | 6.39 |
| | TVD | 5.28 | 5.81 | 6.47 | 7.12 |
| NAD Only | God | 84.98 | 45.52 | 17.57 | 17.43 |
| | TVD | 43.79 | 60.26 | 14.47 | 15.09 |

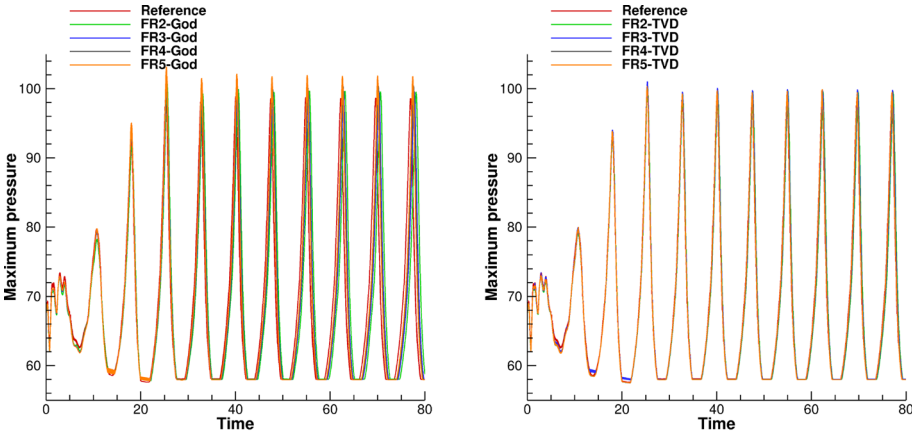


(a) (b)

**Fig. 11** Max pressure time history by different high order FR schemes with the **a** 1st order Godunov subcell FV limiter and **b** 2nd order TVD subcell FV limiter for the slightly unstable detonation problem with the overdriven factor $f = 1.6$

of this problem is slightly unstable in the sense that the detonation front will pulsate around the initial jump position $x_0 = 1.0$ regularly eventually.

Figure 11 shows the peak pressure time history computed by the FR2 to FR5 schemes with different subcell limiters in comparison with the reference solution as mentioned in Sect. 5.5. Figure 11a shows that there are differences in the phases and maximum peaks among the FR2-God to FR5-God results and the reference solution after $t = 40$. Figure 11b shows that both the phases and maximum peaks computed by the FR2-TVD to FR5-TVD schemes agree well with each other and with the reference solution.

We remark that the maximum pressure in the whole computational domain is taken as the peak pressure. But during the simulation, the pressure immediately behind the shock may drop lower than the pressure more away behind the shock, resulting in the "lipped"-shape $p_{\max} - t$ profile in Fig. 11 as explained in [64]. Such "lipped"-shape valleys are also present in similar figures in this paper.

We have also compared the FR2-TVD scheme with the finite difference WENO-JS5 and WENO-Z5 schemes under the same DOFs in Fig. 12. We can see that the FR2-TVD scheme matches better with the reference solution than the other two WENO schemes.

The troubled cell time history of the FR2-TVD scheme is shown in Fig. 13. We can see that the troubled cells are always clustered around the detonation front and swing forth and back in the interval $x \in [0.5, 3.5]$.

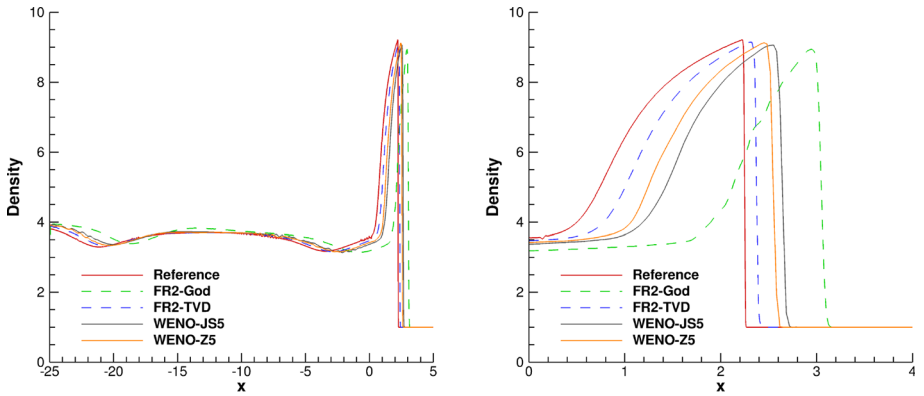


**Fig. 12** Comparison of density profiles at $t = 80$ between various schemes under same DOFs for the slightly unstable detonation problem with $f = 1.6$. The left plot is the view in $[-25, 5]$ and the right is the zoom in $[0, 4]$

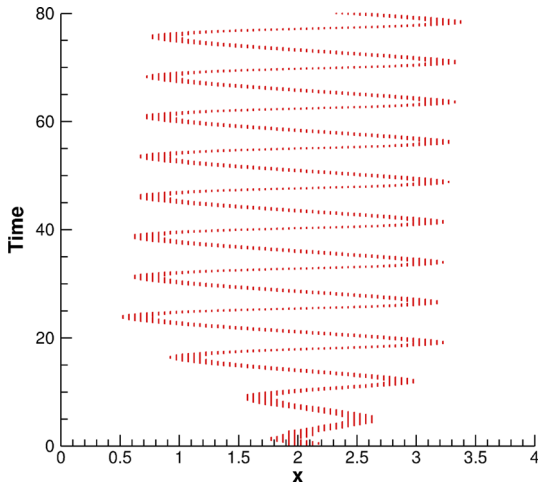


**Fig. 13** Limiter activation history of the FR2-TVD scheme for the slightly unstable detonation problem with $f = 1.6$

### 5.7 Multimode Unstable Detonation Wave with $f = 1.4$

We simulate the detonation problem with the overdriven factor $f = 1.4$ ($A = 411.98$) on the mesh resolution $\delta_{20}$ to the final time $t = 100$, while the parameters $(E_a, q_0, \gamma)$ and computational domain are same as the $f = 1.8$ case in Sect. 5.5. A comparison of the maximum pressure temporal histories between the 1st-order Godunov and 2nd-order TVD subcell FV limiters is shown in Fig. 14. We can observe that the top peaks have a same period but two distinct values. And all the FR schemes produce results in good agreement with the reference solution on the resolution $\delta_{160}$ except the FR2-God scheme which gives larger valley pressures (Fig. 14a). By comparison, the FR schemes with the 2nd-order TVD subcell FV limiter perform better.

The density profiles at $t = 80$ computed with various schemes under same DOFs are shown in Fig. 15. Again, the FR2-TVD scheme gives a better approximation to the reference

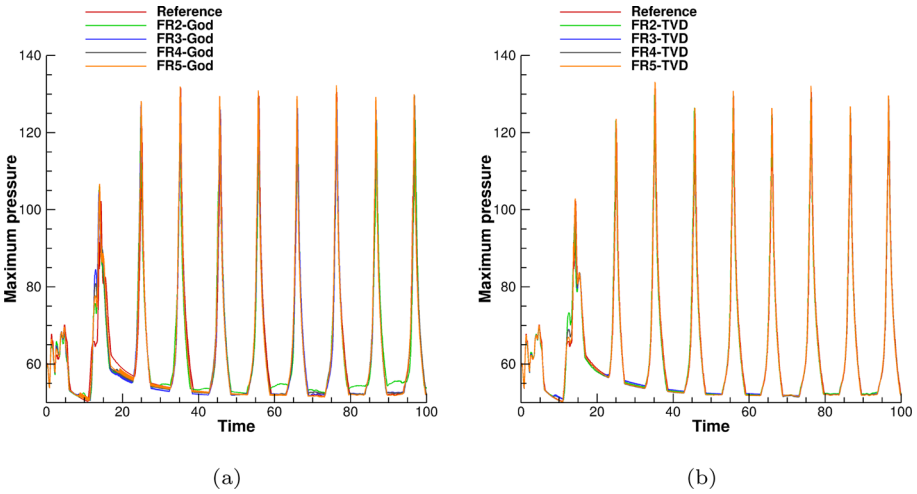


(a) (b)

**Fig. 14** Comparison of the maximum pressure time histories by various FR schemes with **a** the 1st-order Godunov and **b** 2nd-order TVD subcell limiters for the multimode detonation problem with the overdriven factor $f = 1.4$

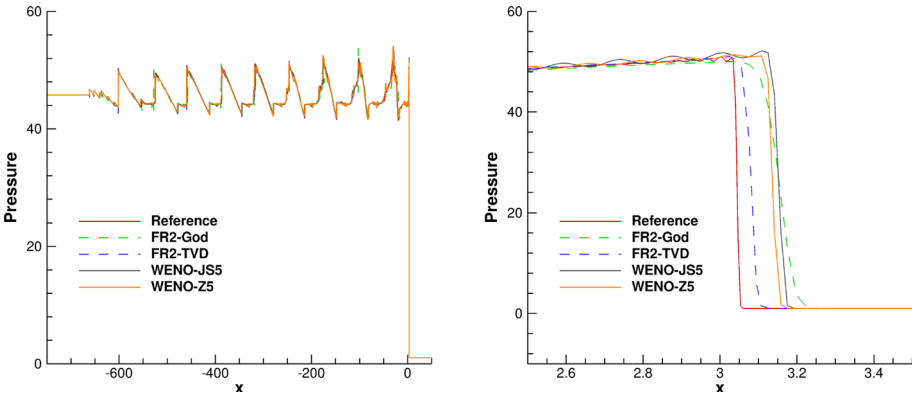


**Fig. 15** Comparison of pressure profiles between various schemes with same DOFs for the multimode detonation problem with $f = 1.4$ at $t = 100$. The right frame is a zoom-in view

solution than the other schemes, while the FR2-God has lower resolution compared with the WENO-JS scheme.

The troubled cell time history by the FR2-TVD scheme is shown in Fig. 16. We see that the initial detonation front will generate spurious left moving compress waves which are marked as troubled cells twice, and which finally develop into a chain of shock waves as shown in the left plot of Fig. 15.

### 5.8 Chaotic Detonation Wave with $f = 1.3$

Finally, we simulate a chaotic detonation problem [61] with the overdriven factor $f = 1.3$ ($A = 583.71$) on the mesh resolution $\delta_{20}$ to the final time $t = 100$. The parameters $(E_a, q_0, \gamma)$ and computational domain are same as in Sect. 5.5. According to the study [61], the solution

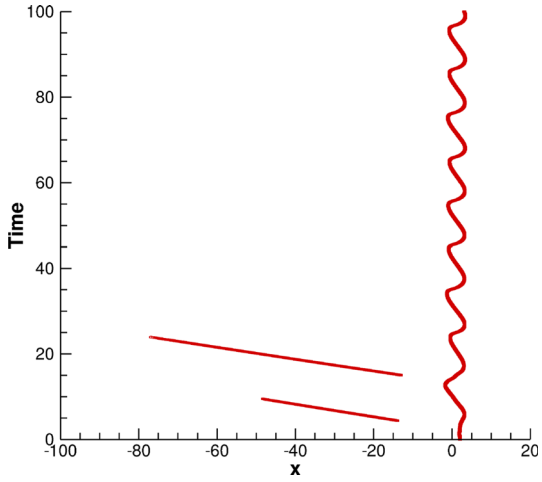


**Fig. 16** Troubled cell time history of FR2-TVD for the multi-mode detonation with $f = 1.4$

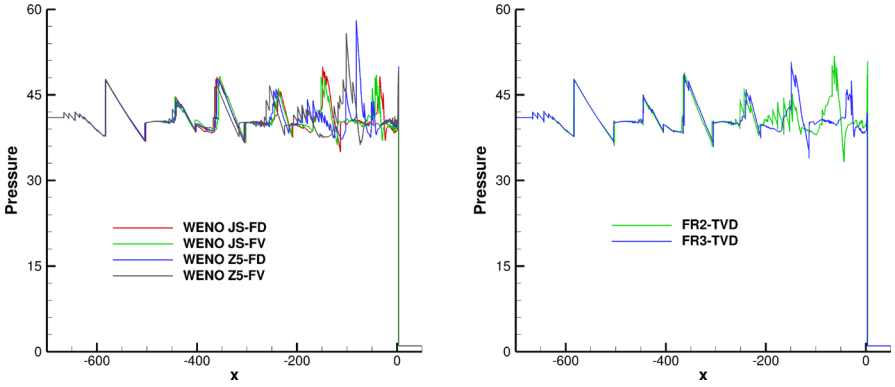


**Fig. 17** Chaotic pressure spatial profiles at $t = 100$ computed by **a** different WENO schemes with the mesh resolution $\delta_{80}$ and **b** FR2-TVD and FR3-TVD schemes with the mesh resolution $\delta_{20}$ for the chaotic detonation with the overdriven factor $f = 1.3$

under this configuration is chaotic, and is sensitive to the initial data such that any small perturbation in the initial data will result in qualitatively similar but quantitatively different shock position time histories. To verify this conclusion, Fig. 17 shows numerical results at $t = 100$ computed by four different characteristic based WENO schemes with the mesh resolution $\delta_{80}$, including finite difference WENO-JS5, alternative finite volume WENO-JS5 [65], finite difference WENO-Z5 and alternative finite volume WENO-Z5 schemes [5], and two FR schemes with the resolution $\delta_{20}$. At the very beginning of the simulation, all the schemes give nearly the same pressure profile, but as time goes on, different schemes produce random distributions near the detonation front, verifying the chaotic property of this problem.

The peak pressure time histories by various FR schemes are shown in Fig. 18. It is seen that the values of the top peaks vary from time to time, and the difference between different orders of FR schemes increases with time. In particular, the result by the FR2-God scheme differs much from other results due to its higher dissipation errors. For completeness, we show the time history of the detected troubled cells in Fig. 19. It is seen that there are troubled cells to

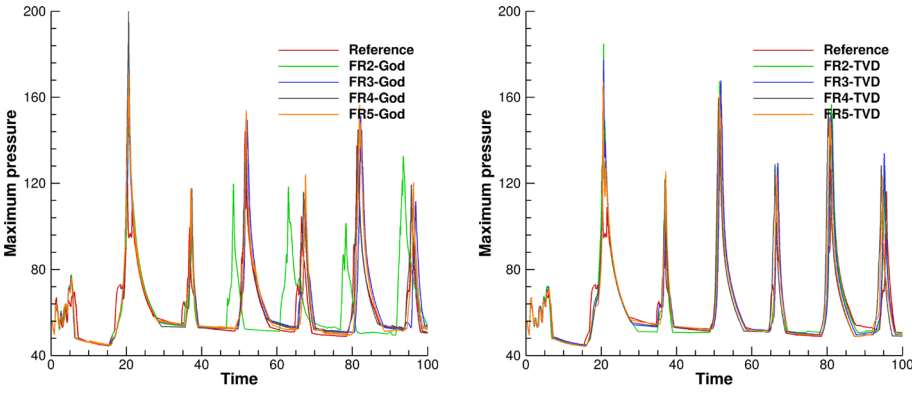


(a) (b)

**Fig. 18** Max pressure time history computed by various FR schemes with **a** 1st-order Godunov and **b** 2nd-order TVD subcell FV limiters for the chaotic detonation problem with $f = 1.3$

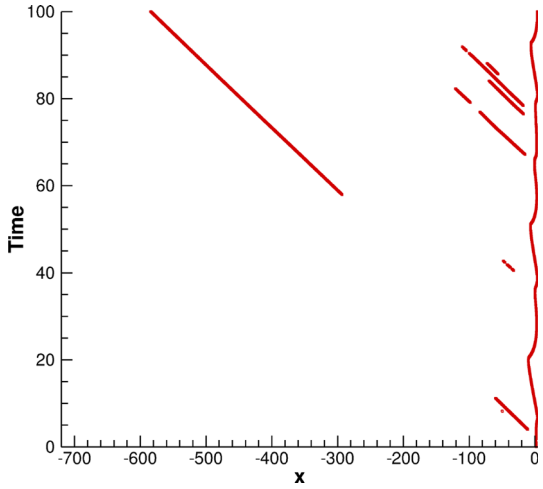


**Fig. 19** Troubled cell time history by the FR2-TVD scheme for the chaotic detonation problem with $f = 1.3$

the left side of the detonation front occasionally, again showing the chaotic property of this problem.

## 6 Conclusion

In this paper, we have presented a modified a posteriori limiting procedure in conjunction with the Vincent-Castonguay-Jameson-Huynh flux reconstruction method and tested the resulting schemes in a couple of one-dimensional detonation problems. In this limiting procedure, the unlimited FR solution at the new time step is first calculated, then it is detected for troubled cells by using the physical admissibility detection (PAD) and numerical admissibility detection (NAD). The solution at the previous time step in the troubled cells are projected into a set of subcell mean values, and a robust finite volume method is used to advance the subcell mean values to the new time step which are finally reconstructed into the FR solution

in the troubled cells. The previous NAD only uses the relaxed discrete maximum principle (DMP). The present NAD uses a KXRCF shock detector prior to the relaxed DMP. The use of the KXRCF detector has two advantages. First, it quickly finds out the very smooth and very discontinuous regions, and by letting these regions bypass the relaxed DMP detection the computer time is reduced. Second, the KXRCF detector can track troubled cells near strong shocks successively in time so as to avoid unnecessary switch between the FR and subcell FV solutions, while the relaxed DMP detection alone will frequently switch, making the solution hard to converge to steady state.

The numerical tests in several one-dimensional detonation wave problems shown that the high order FR schemes with the modified a posteriori limiter are accurate and robust. For example, the FR2-TVD scheme has higher resolution than the WENO-Z5 scheme under same degree of freedoms. In future work, we will extend the present method to multi-dimensional cases.

**Funding** This work is supported by Natural Science Foundation of China (Grant Nos. 91852116, 12071470, 12161141017). The computations are carried out on the high performance computer of the State Key Laboratory of Scientific and Engineering Computing, Chinese Academy of Sciences.

**Data Availability** Enquiries about data availability should be directed to the authors.

## Declarations

**Conflict of interest** The authors declare that they have no conflict of interest.

**Ethical Approval and consent to participate** Not applicable.

**Consent for Publication** Not applicable.

## References

1. Zhu, H.Q., Gao, Z.: An h-adaptive RKDG method with troubled-cell indicator for one-dimensional detonation wave simulations. Adv. Comput. Math. **42**, 1081–1102 (2016). https://doi.org/10.1007/s10444-016-9454-3
2. Henshaw, W.D., Schwendeman, D.W.: An adaptive numerical scheme for high-speed reactive flow on overlapping grids. J. Comput. Phys. **191**(2), 420–447 (2003). https://doi.org/10.1016/S0021-9991(03)00323-1
3. Hu, G.H.: A numerical study of 2D detonation waves with adaptive finite volume methods on unstructured grids. J. Comput. Phys. **331**, 297–311 (2017). https://doi.org/10.1016/j.jcp.2016.11.041
4. Henrick, A.K., Aslam, T.D., Powers, J.M.: Simulations of pulsating one-dimensional detonations with true fifth order accuracy. J. Comput. Phys. **213**(1), 311–329 (2006). https://doi.org/10.1016/j.jcp.2005.08.013
5. Gao, Z., Don, W.S., Li, Z.Q.: High order weighted essentially non-oscillation schemes for one-dimensional detonation wave simulations. J. Comput. Math. **29**(6), 623–638 (2011). https://doi.org/10.4208/jcm.1110-m11si02
6. Wang, C., Zhang, X., Shu, C.-W., Ning, J.G.: Robust high order discontinuous Galerkin schemes for two-dimensional gaseous detonations. J. Comput. Phys. **231**(2), 653–665 (2012). https://doi.org/10.1016/j.jcp.2011.10.002
7. Huynh, H.T.: A flux reconstruction approach to high-order schemes including discontinuous Galerkin methods. In: 18th AIAA Computational Fluid Dynamics Conference, AIAA 2007-4079 (2007)
8. Hesthaven, J.S., Warburton, T.: Nodal Discontinuous Galerkin Methods: Algorithms, Analysis, and Applications. Springer, Berlin (2007)
9. Kopriva, D.A., Kolias, J.H.: A conservative staggered-grid Chebyshev multidomain method for compressible flows. J. Comput. Phys. **125**(1), 244–261 (1996). https://doi.org/10.1006/jcph.1996.0091

10. Liu, Y., Vinokur, M., Wang, Z.J.: Spectral difference method for unstructured grids I: basic formulation. J. Comput. Phys. **216**(2), 780–801 (2006). https://doi.org/10.1016/j.jcp.2006.01.024
11. López-Morales, M.R., Bull, J., Grabill, J., et al.: Verification and validation of HiFiLES: a high-order LES unstructured solver on multi-GPU platforms. In: 32nd AIAA Applied Aerodynamics Conference, AIAA 2014-3168 (2014)
12. Witherden, F.D., Farrington, A.M., Vincent, P.E.: PyFR: An open source framework for solving advection-diffusion type problems on streaming architectures using the flux reconstruction approach. Comput. Phys. Commun. **185**(11), 3028–3040 (2014). https://doi.org/10.1016/j.cpc.2014.07.011
13. Romero, J., Crabill, J., Watkins, J.E., Witherden, F.D., Jameson, A.: ZEFR: A GPU-accelerated high-order solver for compressible viscous flows using the flux reconstruction method. Comput. Phys. Commun. **250**, 107169 (2020). https://doi.org/10.1016/j.cpc.2020.107169
14. Jameson, A.: A proof of the stability of the spectral difference method for all orders of accuracy. J. Sci. Comput. **45**, 348–358 (2010). https://doi.org/10.1007/s10915-009-9339-4
15. Vincent, P.E., Castonguay, P., Jameson, A.: A new class of high-order energy stable flux reconstruction schemes. J. Sci. Comput. **47**, 50–72 (2011). https://doi.org/10.1007/s10915-010-9420-z
16. Wang, Z.J., Gao, H.: A unifying lifting collocation penalty formulation including the discontinuous Galerkin, spectral volume/difference methods for conservation laws on mixed grids. J. Comput. Phys. **228**(21), 8161–8186 (2009). https://doi.org/10.1016/j.jcp.2009.07.036
17. Yu, M.L., Wang, Z.J.: On the connection between the correction and weighting functions in the correction procedure via reconstruction method. J. Sci. Comput. **54**, 227–244 (2013). https://doi.org/10.1007/s10915-012-9618-3
18. Huynh, H.T., Wang, Z.J., Vincent, P.E.: High-order methods for computational fluid dynamics: a brief review of compact differential formulations on unstructured grids. Comput. Fluids **98**, 209–220 (2014). https://doi.org/10.1016/j.compfluid.2013.12.007
19. Godunov, S.K., Bohachevsky, I.: Finite difference method for numerical computation of discontinuous solutions of the equations of fluid dynamics. Matematičeskij sbornik **47**(3), 271–306 (1959)
20. Castonguay, P., Williams, D.M., Vincent, P.E., Jameson, A.: Energy stable flux reconstruction schemes for advection-diffusion problems. Comput. Methods Appl. Mech. Eng. **267**, 400–417 (2013). https://doi.org/10.1016/j.cma.2013.08.012
21. Harten, A.: High resolution schemes for hyperbolic conservation laws. J. Comput. Phys. **49**(3), 357–393 (1983). https://doi.org/10.1016/0021-9991(83)90136-5
22. Sweby, P.K.: High resolution schemes using flux limiters for hyperbolic conservation laws. SIAM J. Numer. Anal. **21**(5), 995–1011 (1984). https://doi.org/10.1137/0721062
23. Cockburn, B., Shu, C.-W.: The Runge-Kutta discontinuous Galerkin method for conservation laws V: multidimensional systems. J. Comput. Phys. **141**(2), 199–224 (1998). https://doi.org/10.1006/jcph.1998.5892
24. Park, J.S., Yoon, S.-H., Kim, C.: Multi-dimensional limiting process for hyperbolic conservation laws on unstructured grids. J. Comput. Phys. **229**(3), 788–812 (2010). https://doi.org/10.1016/j.jcp.2009.10.011
25. Park, J.S., Kim, C.: Hierarchical multi-dimensional limiting strategy for correction procedure via reconstruction. J. Comput. Phys. **308**, 57–80 (2016). https://doi.org/10.1016/j.jcp.2015.12.020
26. Biswas, R., Devine, K.D., Flaherty, J.E.: Parallel, adaptive finite element methods for conservation laws. Appl. Numer. Math. **14**(1), 255–283 (1994). https://doi.org/10.1016/0168-9274(94)90029-9
27. Burbeau, A., Sagaut, P., Bruneau, C.-H.: A problem-independent limiter for high-order Runge-Kutta discontinuous Galerkin methods. J. Comput. Phys. **169**(1), 111–150 (2001). https://doi.org/10.1006/jcph.2001.6718
28. Krivodonova, L.: Limiters for high-order discontinuous Galerkin methods. J. Comput. Phys. **226**(1), 879–896 (2007). https://doi.org/10.1016/j.jcp.2007.05.011
29. Yang, M., Wang, Z.J.: A parameter-free generalized moment limiter for high-order methods on unstructured grids. Adv. Appl. Math. Mech. **1**(4), 451–480 (2009). https://doi.org/10.4208/aamm.09-m0913
30. Qiu, J., Shu, C.W.: Runge-Kutta discontinuous Galerkin method using WENO limiters. SIAM J. Sci. Comput. **26**(3), 907–929 (2005). https://doi.org/10.1137/S1064827503425298
31. Zhu, J., Qiu, J.X., Shu, C.-W., Dumbser, M.: Runge-Kutta discontinuous Galerkin method using WENO limiters II: unstructured meshes. J. Comput. Phys. **227**(9), 4330–4353 (2008). https://doi.org/10.1016/j.jcp.2007.12.024
32. Qiu, J.X., Shu, C.-W.: Hermite WENO schemes and their application as limiters for Runge-Kutta discontinuous Galerkin method: One-dimensional case. J. Comput. Phys. **193**(1), 115–135 (2004). https://doi.org/10.1016/j.jcp.2003.07.026

33. Qiu, J.X., Shu, C.-W.: Hermite WENO schemes and their application as limiters for Runge-Kutta discontinuous Galerkin method II: Two dimensional case. Comput. Fluids **34**(6), 642–663 (2005). https://doi.org/10.1016/j.compfluid.2004.05.005
34. Zhong, X., Shu, C.-W.: A simple weighted essentially nonoscillatory limiter for Runge-Kutta discontinuous Galerkin methods. J. Comput. Phys. **232**(1), 397–415 (2013). https://doi.org/10.1016/j.jcp.2012.08.028
35. Zhang, X., Shu, C.-W.: On maximum-principle-satisfying high order schemes for scalar conservation laws. J. Comput. Phys. **229**(9), 3091–3120 (2010). https://doi.org/10.1016/j.jcp.2009.12.030
36. Zhang, X., Shu, C.-W.: On positivity-preserving high order discontinuous Galerkin schemes for compressible Euler equations on rectangular meshes. J. Comput. Phys. **229**(23), 8918–8934 (2010). https://doi.org/10.1016/j.jcp.2010.08.016
37. Hu, X.Y., Adams, N.A., Shu, C.-W.: Positivity-preserving method for high-order conservative schemes solving compressible Euler equations. J. Comput. Phys. **242**, 169–180 (2013). https://doi.org/10.1016/j.jcp.2013.01.024
38. Clain, S., Diot, S., Loubére, R.: A high-order finite volume method for systems of conservation laws-multi-dimensional optimal order detection (MOOD). J. Comput. Phys. **230**(10), 4028–4050 (2011). https://doi.org/10.1016/j.jcp.2011.02.026
39. Diot, S., Clain, S., Loubére, R.: Improved detection criteria for the multi-dimensional optimal order detection (MOOD) on unstructured meshes with very high-order polynomials. Comput. Fluids **64**, 43–63 (2012). https://doi.org/10.1016/j.compfluid.2012.05.004
40. Dumbser, M., Zanotti, O., Loubére, R., Diot, S.: A posteriori subcell limiting of the discontinuous Galerkin finite element method for hyperbolic conservation laws. J. Comput. Phys. **278**, 47–75 (2014). https://doi.org/10.1016/j.jcp.2014.08.009
41. Sonntag, M., Munz, C.-D.: Shock capturing for discontinuous Galerkin methods using finite volume subcells. In: Fuhrmann, J., Ohlberger, M., Rohde, C. (eds.) Finite Volumes for Complex Applications VII-Elliptic, Parabolic and Hyperbolic Problems, pp. 945–953. Springer, Cham (2014)
42. Vilar, F.: A posteriori correction of high-order discontinuous Galerkin scheme through subcell finite volume formulation and flux reconstruction. J. Comput. Phys. **387**, 245–279 (2019). https://doi.org/10.1016/j.jcp.2018.10.050
43. Li, Y., Wang, Z.J.: Recent progress in a convergent and accuracy preserving limiter for the FR/CPR method. AIAA 2017-0756 (2017). https://doi.org/10.2514/6.2017-0756
44. Krivodonova, L., Xin, J., Remacle, J.-F., Chevaugeon, N., Flaherty, J.E.: Shock detection and limiting with discontinuous Galerkin methods for hyperbolic conservation laws. Appl. Numer. Math. **48**(3), 323–338 (2004). https://doi.org/10.1016/j.apnum.2003.11.002
45. Vincent, P.E., Castonguay, P., Jameson, A., Huynh, H.T.: Insights from von Neumann analysis of high-order flux reconstruction schemes. J. Comput. Phys. **230**(22), 8134–8154 (2011). https://doi.org/10.1016/j.jcp.2011.07.013
46. Jameson, A., Vincent, P.E., Castonguay, P.: On the non-linear stability of flux reconstruction schemes. J. Sci. Comput. **50**, 434–445 (2012). https://doi.org/10.1007/s10915-011-9490-6
47. Witherden, F.D., Vincent, P.E.: On nodal point sets for flux reconstruction. J. Comput. Appl. Math. **381**, 113014 (2021). https://doi.org/10.1016/j.cam.2020.113014
48. Toro, E.: Riemann Solvers and Numerical Methods for Fluid Dynamics: A Practical Introduction. Springer, USA (2009). https://doi.org/10.1007/b79761
49. Pan, J.H., Ren, Y.X.: High order sub-cell finite volume schemes for solving hyperbolic conservation laws I: basic formulation and one-dimensional analysis. Sci. China Phys. Mech. Astron. **60**(8), 084711 (2017). https://doi.org/10.1007/s11433-017-9033-9
50. Runge, C.: Über empirische funktionen und die interpolation zwischen äquidistanten ordinaten. Z. Angew. Math. Phys. **46**, 224–243 (1901)
51. Godunov, S.K.: A difference method for numerical calculation of discontinuous solutions of the equations of hydrodynamics. Math. Sbornik Novaya Seriya **47**(3), 271–306 (1959)
52. van Leer, B.: Towards the ultimate conservative difference scheme. V. A second-order sequel to Godunov's method. J. Comput. Phys. **32**(1), 101–136 (1979). https://doi.org/10.1016/0021-9991(79)90145-1
53. Harten, A., Osher, S.: Uniformly high-order accurate nonoscillatory schemes I. SIAM J. Numer. Anal. **24**(2), 279–309 (1987). https://doi.org/10.1137/0724022
54. Gao, Z., Don, W.S., Li, Z.Q.: High order weighted essentially non-oscillation schemes for two-dimensional detonation wave simulations. J. Sci. Comput. **53**, 80–101 (2012). https://doi.org/10.1007/s10915-011-9569-0
55. Zhang, Z.C., Yu, S.-T., He, H., Chang, S.-C.: Direct calculations of two-and three-dimensional detonations by an extended CE/SE method. AIAA 2001-0476 (2001). https://doi.org/10.2514/6.2001-476

56. Wang, B., He, H., Yu, S.-T.: Direct calculation of wave implosion for detonation initiation. AIAA J. **43**(10), 2157–2169 (2005). https://doi.org/10.2514/1.11887
57. Shu, C.-W., Osher, S.: Efficient implementation of essentially non-oscillatory shock-capturing schemes. J. Comput. Phys. **77**(2), 439–471 (1988). https://doi.org/10.1016/0021-9991(88)90177-5
58. Sod, G.A.: A survey of several finite difference methods for systems of nonlinear hyperbolic conservation laws. J. Comput. Phys. **27**(1), 1–31 (1978). https://doi.org/10.1016/0021-9991(78)90023-2
59. Einfeldt, B., Munz, C.D., Roe, P.L., Sjögreen, B.: On Godunov-type methods near low densities. J. Comput. Phys. **92**(2), 273–295 (1991). https://doi.org/10.1016/0021-9991(91)90211-3
60. Woodward, P., Colella, P.: The numerical simulation of two-dimensional fluid flow with strong shocks. J. Comput. Phys. **54**(1), 115–173 (1984). https://doi.org/10.1016/0021-9991(84)90142-6
61. Bourlioux, A., Majda, A.J., Roytburd, V.: Theoretical and numerical structure for unstable one-dimensional detonations. SIAM J. Appl. Math. **51**(2), 303–343 (1991). https://doi.org/10.1137/0151016
62. Di, Y.N., Hu, G.H., Li, R., Yang, F.: On accurately resolving detonation dynamics by adaptive finite volume method on unstructured grids. Commun. Comput. Phys. **29**(2), 445–471 (2020). https://doi.org/10.4208/cicp.OA-2020-0028
63. Deiterding, R.: Parallel adaptive simulation of multi-dimensional detonation structures. PhD thesis, Brandenburgische Technische Universitat Cottbus (2003). https://eprints.soton.ac.uk/380602/
64. Karagozian, P., Hwang, P., Fedkiw, R., Merriman, B., Karagozian, A., Osher, S.: Numerical resolution of pulsating detonation waves. Combustion Theory and Modelling **4** (1970). https://doi.org/10.1088/1364-7830/4/3/301
65. Jiang, Y., Shu, C.-W., Zhang, M.P.: An alternative formulation of finite difference weighted ENO schemes with Lax-Wendroff time discretization for conservation laws. SIAM J. Sci. Comput. **35**, 1137–1160 (2013). https://doi.org/10.1137/120889885